Dynamic Compressive Response of Stainless-Steel Square Honeycombs

D. D. Radford

G. J. McShane

V. S. Deshpande

N. A. Fleck[1]
e-mail: naf1@eng.cam.ac.uk

Department of Engineering,
University of Cambridge,
Trumpington Street,
Cambridge, CB2 1PZ,
United Kingdom

The dynamic out-of-plane compressive response of stainless-steel square honeycombs has been investigated for impact velocities ranging from quasi-static values to 300 ms^{-1}. *Square-honeycomb specimens of relative density* 0.10 *were manufactured using a slotting technique, and the stresses on the front and back faces of the dynamically compressed square honeycombs were measured using a direct impact Kolsky bar. Three-dimensional finite element simulations of the experiments were performed to model the response and to help interpret the experimental results. The study has identified three distinct factors governing the dynamic response of the square honeycombs: material rate sensitivity, inertial stabilization of the webs against buckling, and plastic wave propagation. Material rate sensitivity and inertial stabilization of the webs against buckling cause the front and back face stresses to increase by about a factor of two over their quasi-static value when the impact speed is increased from 0 to* 50 ms^{-1}. *At higher impact velocities, plastic wave effects cause the front face stress to increase linearly with velocity whereas the back face stress is almost independent of velocity. The finite element predictions are in reasonable agreement with the measurements.* [DOI: 10.1115/1.2424717]

Keywords: honeycomb cores, impact testing, dynamic loads, material rate dependence, dynamic buckling

1 Introduction

Several recent investigations have revealed that metallic sandwich panels have an advantage over monolithic plates of equal mass in blast resistant structural applications [1–4]. The dynamic performance of sandwich panels is strongly dependent upon their core topology and the square-honeycomb core is a promising candidate [1,2]. The present study is a combined experimental and numerical investigation of the dynamic out-of-plane compressive response of square honeycombs in a sandwich configuration.

The out-of-plane compression of aluminium hexagonal honeycombs under low speed impact is fairly well understood. In the automotive industry, the focus of attention has been on the energy absorption capacity of the hexagonal honeycomb of relative density $0.01 \leq \bar{\rho} < 0.04$ subject to impact speeds v_o below 30 ms^{-1}. At these speeds, the dynamic strength enhancement of the honeycombs is primarily due to inertial stabilization of the honeycomb webs against elastic buckling: the honeycombs are in axial equilibrium and, consequently, the forces on the impacted and distal ends are approximately equal; see for example Zhao and Gary [5] and Wu and Jiang [6]. There exists little experimental data on the dynamic compression of honeycombs at high speeds ($v_o > 100$ ms^{-1}) apart from the investigation by Harrigan et al. [7] on the dynamic crushing of aluminium hexagonal honeycombs of relative density $\bar{\rho} \approx 1\%$. They measured the stresses on the impacted end of these specimens and concluded that plastic wave effects lead to an elevation in the dynamic plateau strength.

An optimization study by Xue and Hutchinson [2] has revealed that square honeycombs with relatively densities of about 10%, and made from stainless steel (which displays a strong strain hardening response) are promising for applications in blast resistant sandwich plates. The honeycombs of interest in such blast applications are different from those considered by Harrigan et al. [7]: they have higher relative densities and are made from a material with a high strain hardening capacity. Xue and Hutchinson [8] have recently reported finite element simulations of the dynamic response of such stainless steel square honeycombs subjected to compressive velocities in the range 20–200 ms^{-1}. Their simulations highlighted three factors contributing to the dynamic strength enhancement of the stainless steel square honeycombs: material rate sensitivity, inertial stabilization of the webs against buckling, and plastic wave propagation. For the loading rates of interest in blast applications, they argued that plastic wave propagation and plastic buckling occur over comparable timescales, and substantial axial plastic straining can occur prior to the onset of buckling.

The current study is an experimental validation of the findings of Xue and Hutchinson [8], and has the following scope. The dynamic out-of-plane compressive response of square-honeycomb lattice material is investigated for applied compressive velocities ranging from quasi-static values to 300 ms^{-1}. The stresses on the impacted and distal ends of $\bar{\rho} = 0.10$ stainless-steel square honeycombs are measured using a direct impact Kolsky bar, and high-speed photography is employed to observe the dynamic deformation modes. The effect of specimen height is explored by performing tests on specimens of height $H = 6$ mm and 30 mm. The experimental measurements are compared with three-dimensional finite element simulations to gauge the fidelity of the simulations and to help interpret the experimental findings.

2 Experimental Investigation

2.1 Specimen Configuration and Manufacture. Square honeycombs have been manufactured from AISI type 304 stainless steel sheets of thickness $b = 0.30$ mm using the technique developed by Côté et al. [9]. The sheets were cropped into rectangles of height H equal to 6 mm and 30 mm, and length 21 mm. Cross-slots (Fig. 1) of width $\Delta b = 0.31$ mm, and spacing $L = 6$ mm, were cut by electro-discharge machining (EDM) and the square honeycomb was assembled as sketched in Fig. 1. A clearance of 10 μm between sheet and slot allowed for easy assembly while providing

[1]Corresponding author.

Contributed by the Applied Mechanics Division of ASME for publication in the JOURNAL OF APPLIED MECHANICS. Manuscript received January 20, 2006; final manuscript received May 9, 2006. Review conducted by Robert M. McMeeking.

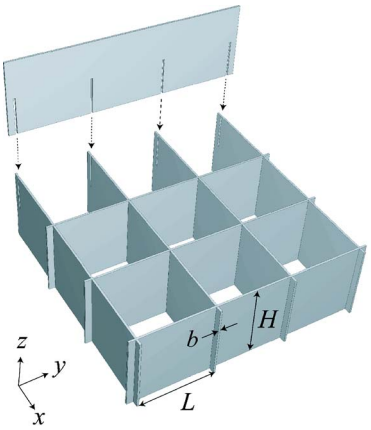

$L = 6$ mm
$H = 6$ mm and 30 mm
$b = 0.3$ mm

Fig. 1 Sketch of the manufacturing technique for the square honeycomb

a sufficiently tight fit to assure stability. Brazing was conducted with Ni-Cr 25-P10 (wt %) at a temperature of 1120°C in an atmosphere of dry argon at 0.03–0.1 mbar, and the braze was applied uniformly over the sheets. Capillarity draws the braze into the joints, and results in an excellent bond. All specimens comprised 3×3 cells and had dimensions 21 mm$\times$21 mm$\times H$. The relative density of the square-honeycomb is to first order in b/L given by

$$\bar{\rho} = \frac{2b}{L} \tag{1}$$

giving a relative density of 10%. This was confirmed by weighing the specimens.

2.2 Properties of the Constituent Materials. The uniaxial tensile response of the AISI 304 stainless steel used to manufacture the square honeycomb specimens was measured at a nominal strain rate of 10^{-3} s^{-1}, and the true tensile stress versus logarithmic strain curve is plotted in Fig. 2(*a*). This material was tested in the "as-brazed" condition to match that of the as-manufactured specimens, and the measured 0.2% offset yield strength σ_Y and ultimate tensile strength σ_{UTS} were 300 MPa and 700 MPa, respectively. Post-yield, the stainless steel exhibits a linear hardening response with a tangent hardening modulus $E_t \approx 1.4$ GPa.

Stout and Follansbee [10] have investigated the strain-rate sensitivity of the AISI 304 stainless steel for strain rates in the range 10^{-4} s$^{-1} < \dot{\varepsilon} < 10^{4}$ s^{-1}. Their data are replotted in Fig. 2(*b*), where the dynamic strength enhancement ratio R is plotted against the plastic strain rate $\dot{\varepsilon}^p$ for 10^{-3} s$^{-1} < \dot{\varepsilon}^p < 10^{4}$ s^{-1}. Here, R is defined as the ratio of the stress $\sigma_d(\varepsilon^p=0.1)$ at an applied strain rate $\dot{\varepsilon}^p$ to the stress $\sigma_0(\varepsilon^p=0.1)$ at the quasi-static rate $\dot{\varepsilon}^p = 10^{-3}$ s^{-1}. The measured stress versus strain histories presented by Stout and Follansbee [10] indicate that R is reasonably independent of the level of plastic strain ε^p at which R is calculated. Thus, the dynamic strength σ_d versus plastic strain ε^p history can be estimated from the relation

$$\sigma_d(\varepsilon^p) = R(\dot{\varepsilon}^p)\sigma_0(\varepsilon^p) \tag{2}$$

where $R(\dot{\varepsilon}^p)$ is given in Fig. 2(*b*). In the finite element simulations of the experiments presented below, we employ this prescription for the strain-rate sensitivity of the 304 stainless steel, with $\sigma_0(\varepsilon^p)$ given by the measured quasi-static ($\dot{\varepsilon} = 10^{-3}$ s^{-1}) stress versus strain history (Fig. 2(*a*)). As an example, the estimated true tensile stress versus logarithmic strain histories of the AISI 304 stainless steel at three selected additional values of applied strain rate are included in Fig. 2(*a*).

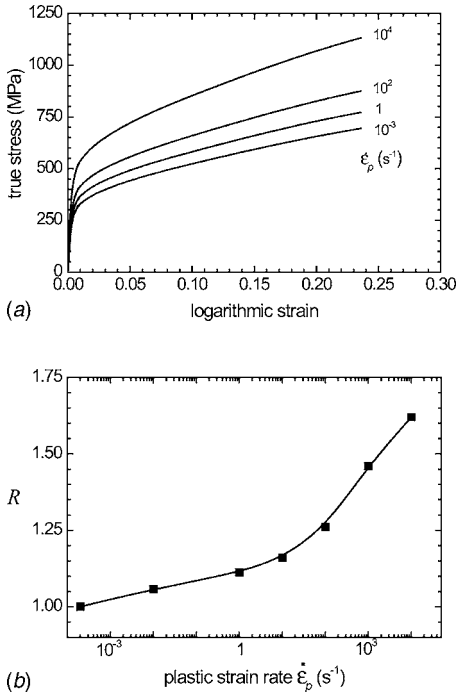

Fig. 2 (*a*) The measured quasi-static tensile stress versus strain response of the AISI 304 stainless steel and the estimated high strain rate response at three additional values of the applied strain rate using the data of Stout and Follansbee [10]. (*b*) The dynamic strength enhancement ratio R as a function of plastic strain rate $\dot{\varepsilon}^p$ for the AISI 304 stainless steel at a plastic strain $\varepsilon^p = 0.1$ [10].

2.3 Quasi-static Compressive Response of the Square Honeycombs. The quasi-static compressive response of the square honeycombs was measured in a screw-driven test machine at an applied nominal strain rate of 10^{-3} s^{-1}. A laser extensometer was employed to measure the average nominal compressive strain ε while the nominal stress σ was inferred from the measurements from the load cell of the test machine.

The measured out-of-plane quasi-static compressive responses of the square-honeycomb specimens are plotted in Fig. 3. The specimens display a peak strength followed by softening and, finally, rapid hardening upon densification at a strain $\varepsilon_D \approx 0.6$–$0.7$. Note that the $H=30$ mm specimen has a lower peak strength and displays more abrupt softening. Côté et al. [9] have already noted that the quasi-static collapse mode involves tor-

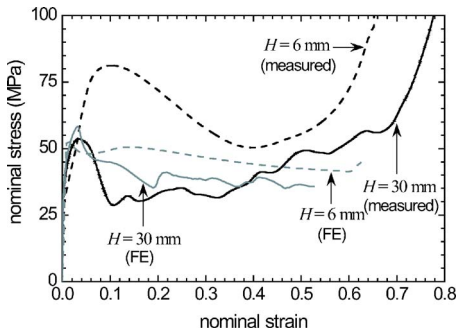

Fig. 3 Quasi-static compressive stress versus strain response of the $\bar{\rho}=0.10$ square honeycombs, of cell height $H=6$ mm and $H=30$ mm

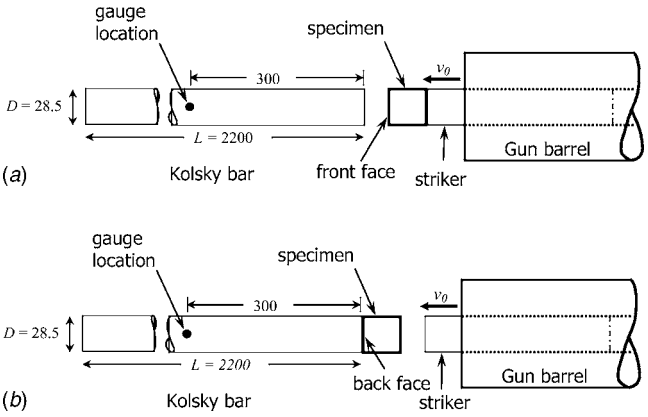

Fig. 4 Sketches of the direct impact Kolsky bar setup for measuring the stress versus time histories in (*a*) front face and (*b*) back face configurations. All dimensions are in mm.

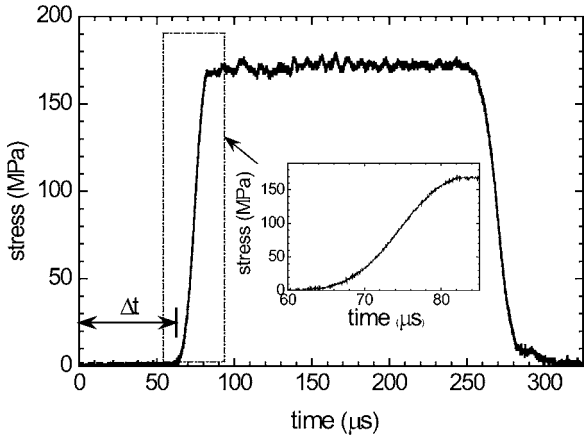

Fig. 5 Stress versus time history measured in the Kolsky bar during a calibration test. A 0.5 m long steel striker is fired at the Kolsky bar at v_o=9.0 ms^{-1}.

sional plastic buckling of the cells, with the peak static strength σ_s accurately predicted by a plastic bifurcation analysis [9].

2.4 Dynamic Test Protocol. The dynamic out-of-plane compressive response of the square honeycombs was measured from a series of direct impact tests in which the forces on the faces of the honeycomb were measured via a strain-gauged Kolsky bar [11]. Two types of tests were conducted to measure the forces on the impacted and distal ends of the specimens, referred to subsequently as the front and back faces, respectively.

In the front face configuration (Fig. 4(*a*)), the test specimen is attached to one end of the striker bar (sometimes known as the backing mass, [7]) and the combined striker bar and specimen are fired from a gas gun so that the specimen impacts the Kolsky bar normally and centrally. In the back face configuration (Fig. 4(*b*)), the specimen is placed centrally on the stationary Kolsky bar and the striker bar is fired from the gas gun and impacts the specimen. These two independent tests allow for a measurement of the transient force on both the impacted and distal faces of the specimen.

The kinetic energy of the projected striker governs the level of compression attained and the imposed transient velocity at one end of the specimen. We wished to compress the specimens at approximately constant velocity and chose the striker masses accordingly. In the experiments conducted at low velocity ($v_o \leqslant 50$ ms^{-1}) and at intermediate velocity (50 ms$^{-1} < v_o < 200$ ms^{-1}) strikers of mass M=2.4 kg and 0.5 kg, respectively, were employed. A striker of mass M=0.090 kg sufficed for the high velocity $v_o \geqslant 200$ ms^{-1} experiments. The measurements and finite element simulations presented below show that these striker masses are sufficient to provide almost constant velocity compression of the square-honeycomb specimens for nominal compressive strains of up to 40%.

The striker was given the required velocity by firing it from a gas gun of barrel length 4.5 m and diameter 28.5 mm. No sabot was employed as the cylindrical striker had a diameter equal to 28.0 mm. The bursting of copper shim diaphragms formed the breech mechanism of the gun. The impact experiments were performed at velocities ranging from approximately 10 ms^{-1} to 300 ms^{-1}. The velocity of the projectile was measured at the exit of the barrel using laser-velocity gates and the impacted end of the Kolsky bar was placed 100 mm from the open end of the gun barrel.

The setup of the Kolsky pressure bar [11] is standard. A circular cylindrical bar of length 2.2 m and diameter 28.5 mm was made from the maraging steel M-300 (yield strength 1900 MPa). The pressure history on the impacted end of the bar was measured by diametrically opposite axial strain gauges placed approximately 10 diameters from the impact end of the bar. The elastic strain histories in the bars were monitored using the two 120 Ω TML foil gauges of gauge length 1 mm in a half-Wheatstone bridge configuration. A strain bridge amplifier of cutoff frequency 500 kHz was used to provide the bridge input voltage and a digital storage oscilloscope was used to record the output signal. The bridge system was calibrated dynamically over the range of strains measured during the experiments and was accurate to within 3%. The longitudinal elastic wave speed was measured at 4860 ms^{-1}, giving a time window of 800 μs before elastic reflections from the distal end of the bar complicated the measurement of stress.

The response time and accuracy of the measurement system were gauged from a series of calibration tests. We report the results of one such representative test as follows. A maraging steel striker bar of diameter 28.5 mm and length 0.5 m was fired at the Kolsky bar at a velocity v_o=9.0 ms^{-1}. The stress versus time response measured by the strain gauges on the Kolsky bar is plotted in Fig. 5. With time t=0 corresponding to the instant of impact, the stress pulse arrives at the gauge location at t=66 μs. Elastic wave theory predicts that the axial stress in the bar is $\rho c v_o/2$ =175 MPa, where ρ and c are the density and longitudinal elastic wave speed of steel, respectively. The measured peak value of the stress is within 1% of this prediction. However, the measurement system has a finite response time, with the stress rising to this peak value in approximately 10 μs (see the inset in Fig. 5). This rise time places an operational limit on measuring the dynamic response of the square honeycombs. It becomes significant at the higher velocities because significant compression of the specimen is achieved within the first 10 μs. The measured stress in the calibration test drops back to zero at t=270 μs; this is the time for propagation of an axial stress wave down the bar, followed by reflection of the elastic wave from the distal end of the striker bar back to the strain gauge.

3 Experimental Results for the Dynamic Compression of Square Honeycombs

We first present the dynamic compression response of the H =30 mm square-honeycomb specimens and then contrast these measurements with those for the H=6 mm specimens.

3.1 The H=30 mm Square Honeycombs. The measured front and back face axial stress versus normalized time $\bar{t} \equiv v_o t/H$ histories for the H=30 mm specimens are presented in Figs. 6(*a*), 7(*a*), and 8(*a*) for impact velocities v_o=20 ms^{-1}, 50 ms^{-1}, and 240 ms^{-1}, respectively. The time t is measured from the instant of impact and thus the normalized time $\bar{t}$ is a measure of the nominal compressive strain of the square-honeycomb speci-

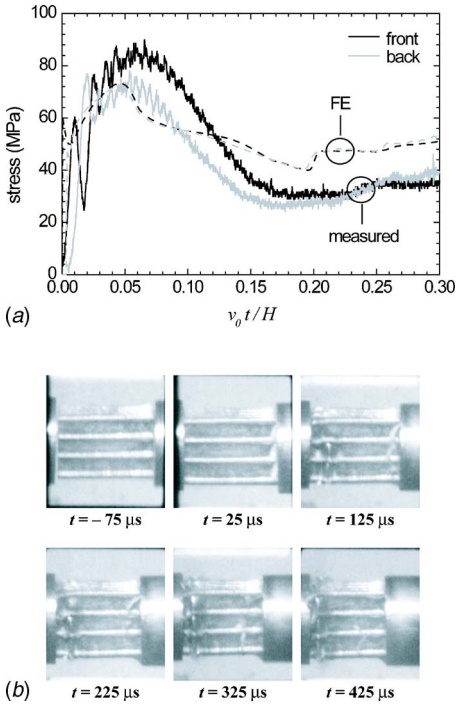

Fig. 6 (*a*) Measured front and back face stress versus normalised time histories in the H=30 mm honeycomb specimens impacted at v_o=20 ms^{-1}; and (*b*) the corresponding high speed photographic sequence of the deformation in the front face configuration at an interframe time of 100 μs. The finite element predictions (constant velocity boundary condition) are included in (*a*).

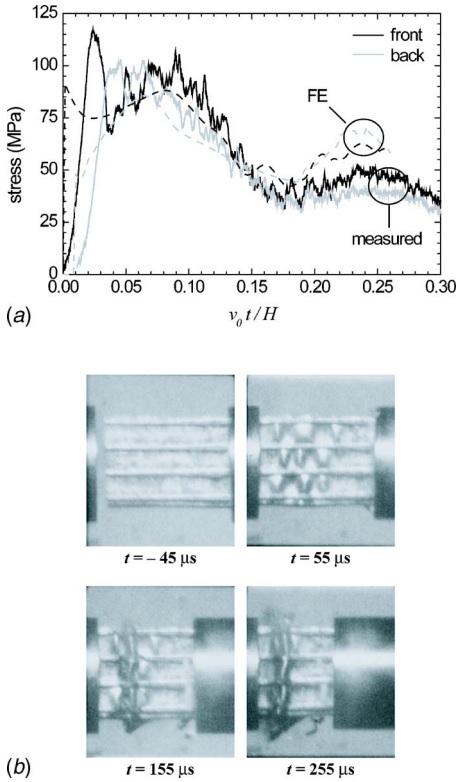

Fig. 7 (*a*) Measured front and back face stress versus normalised time histories in the H=30 mm honeycomb specimens impacted at v_o=50 ms^{-1}; and (*b*) the corresponding high speed photographic sequence of the deformation in the front face configuration at an interframe time of 100 μs. The finite element predictions (constant velocity boundary condition) are included in (*a*).

mens, assuming compression at a uniform velocity v_o over the deformation history. In these figures, the front and back face stresses are defined from the measured front face force F_f and back face force F_b as

$$\sigma_f \equiv \frac{F_f}{A_o} \tag{4a}$$

and

$$\sigma_b \equiv \frac{F_b}{A_o} \tag{4b}$$

respectively, where $A_o = 21 \times 21$ mm^2 is the cross-sectional area of the square-honeycomb specimens. High-speed photographic sequences of the deformation of the specimens in the front face configuration are given in Figs. 6(*b*), 7(*b*), and 8(*b*). The interframe times in Figs. 6(*b*) and 7(*b*) are 100 μs while the sequences in Fig. 8(*b*) were taken at 40 μs intervals. The exposure time of each photograph is 20% of the interframe time in all cases. The dust clouds in the high-speed photographs are associated with tearing of the square honeycombs along the brazed joints. This was confirmed by post-test visual inspections of the dynamically tested specimens. (Tearing of the joints was also observed in the quasi-static tests.) The dynamic measurements show two qualitatively distinct behaviors: (1) the response for v_o=20 ms^{-1} and 50 ms^{-1}, and (2) the response for v_o=240 ms^{-1}.

1. v_o=20 ms^{-1} and 50 ms^{-1}. The measured front and back face stresses equalize within $t \approx 10$ μs (or $v_o t/H = 0.01-0.02$). Recall that the response time of the measurement system is 10 μs. Thus, the early differences between the front and back face stresses are likely to be associated with the measurement system and we conclude that the specimens are in axial equilibrium over almost the entire deformation history. Similar to the quasi-static case, the square-honeycomb specimens have a distinct stress peak. These peak stresses increase with impact velocity and at v_o=50 ms^{-1} they are approximately twice the quasi-static value. Material strain rate sensitivity alone cannot account for the increase in the peak stress and dynamic stabilization of the webs against buckling is expected to play an important role.
2. v_o=240 ms^{-1}. The measured front face stress is approximately constant over the deformation history (to within "ringing" of the measurements) up to the specimen densification strain of $v_o t/H \approx 0.9$. Moreover, the front face stress exceeds the back face stress over the deformation history. This indicates that the specimen is not in equilibrium, with wave propagation effects playing a dominant role. This is substantiated by the high-speed photographs (Fig. 8(*b*)): shortening of the specimen is concentrated near the impacted end, with the distal end of the specimen undergoing only small plastic deformations.

The measured peak front face stress σ_f^p and back face stress σ_b^p are normalized by the peak quasi-static value σ_s and are plotted in Fig. 9 as a function of the impact velocity v_o. Over the range $0 < v_o < 50$ ms^{-1}, the front and back face stresses remain equal and attain double their quasi-static values. For $v_o > 50$ ms^{-1}, the back face stress remains approximately constant at its value for $v_o = 50$ ms^{-1} while the front face stress increases approximately linearly with velocity. These observations suggest that the following three mechanisms provide the dynamic strength enhancements in these experiments.

1. Material strain rate sensitivity. The dynamic strength en-

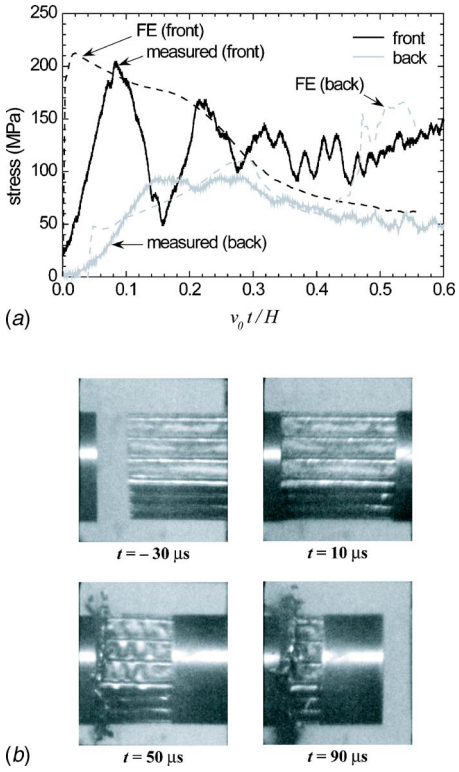

Fig. 8 (*a*) Measured front and back face stress versus normalised time histories in the $H=30$ mm honeycomb specimens impacted at $v_o=240$ ms^{-1}; and (*b*) the corresponding high speed photographic sequence of the deformation in the front face configuration at an inter-frame time of 40 μs. The finite element predictions (constant velocity boundary condition) are included in (*a*).

hancement of the square honeycombs due to the material strain rate is estimated from the measurements of Stout and Follansbee [10] by assuming uniform compression of the square honeycombs at a rate $\dot{\varepsilon}^p = v_o/H$. The strength enhancement ratio $R(\dot{\varepsilon}^p)$ is plotted versus impact velocity in Fig. 9. Comparisons with the measured dynamic strength enhancement ratios σ_b^p/σ_s and σ_f^p/σ_s suggest that the stress enhancements for $v_o < 20$ ms^{-1} are largely due to the material strain rate sensitivity. Material rate sensitivity cannot, however, account for the strength enhancements at the higher velocities.

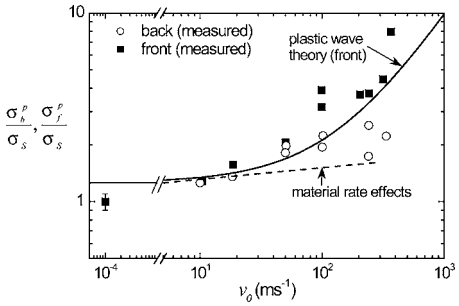

Fig. 9 Measured peak front face stress σ_f^p and back face stress σ_b^p versus impact velocity v_o in the $H=30$ mm honeycomb specimens. The measured dynamic stresses are normalized by peak quasi-static stress σ_s from Fig. 3. The predictions of the dynamic stresses based on material strain-rate sensitivity and one-dimensional plastic wave propagation are included.

2. Dynamic buckling. As discussed in Section 2.3, the peak quasi-static strength of the square honeycombs is set by torsional plastic buckling of the cells of the square honeycomb. Under dynamic loading, inertial stabilization results in an enhanced buckling strength due to the activation of higher order buckling modes. Abrahmson and Goodier [12] and Calladine and English [13] have elaborated on this in the case for rods which have attained axial equilibrium. This higher order buckling is clearly seen in the high-speed photographs in Fig. 8(*b*). In the velocity range $20 \text{ ms}^{-1} < v_o < 50 \text{ ms}^{-1}$, the front and back face stresses are approximately equal but material rate sensitivity alone cannot account for the dynamic strength enhancement. The additional strengthening is attributed to the enhanced dynamic buckling strength of the square honeycombs due to inertial stabilization.
3. Plastic wave propagation. At high impact velocities, a plastic wave moves along the prismatic axis of the honeycomb. Prior to the onset of buckling of the webs of the square honeycombs, one-dimensional elastic–plastic wave theory can be used to estimate dynamic stress on the front face of the honeycomb as the wave propagates through the thickness of the honeycomb. In the small strain, rate-independent limit, the front face stress is given by

$$\sigma_f = \frac{F_f}{A_o} = \sigma_Y \bar{\rho} + \rho_c c_{\text{pl}} \left(v_o - \frac{\sigma_Y}{\rho_s c_e} \right) \approx \sigma_Y \bar{\rho} + \rho_c c_{\text{pl}} v_o \quad (5)$$

where c_e and c_{pl} are the elastic and plastic wave speeds, respectively, of the honeycomb parent material of yield strength σ_Y. The density of the honeycomb is $\rho_c \equiv \bar{\rho}\rho_s$ in terms of the density ρ_s of the parent material. During propagation of the plastic wave to the back face, the back face stress has no inertial contribution and is given by $\sigma_b = \sigma_Y \bar{\rho}$. It remains to specify an appropriate value for σ_Y in order to determine σ_f and σ_b. Here we arbitrarily take σ_Y to be the yield strength of the solid material at a strain rate $\dot{\varepsilon}^p = 10^4$ s^{-1} (the nominal strain rate for a honeycomb of height $H=30$ mm compressed at $v_o = 300$ ms^{-1}) in order to illustrate the predictions of the one-dimensional wave model, and plot Eq. (5) with $c_{\text{pl}} \equiv \sqrt{E_t/\rho_s} \approx 410$ ms^{-1} in Fig. 9. The good agreement of the front face stress prediction with the experimental measurements for $v_o > 50$ ms^{-1} suggests that one-dimensional plastic wave propagation sets the peak front face stresses at these higher velocities.

3.2 The Effect of Specimen Height. The measured front and back face stress versus time histories of the $H=30$ mm and $H=6$ mm square-honeycomb specimens for an impact velocity $v_o = 100$ ms^{-1} are plotted in Figs. 10(*a*) and 10(*b*), respectively. Plastic wave effects play a significant role in the $H=30$ mm specimen with the front and back face forces equalizing only for $v_o t/H > 0.1$. Recall that the plastic wave speed in 304 stainless steel is $c_{\text{pl}} \approx 410$ ms^{-1}. Thus, we expect the plastic wave to reach the rear face at the longer time $v_o t/H \approx 0.25$. The finite element calculations reported subsequently show that material rate sensitivity results in the specimen attaining axial equilibrium sooner than estimated from a rate independent plastic wave theory due to an "increased" plastic wave speed resulting from smearing out of the plastic shock. (The width of the shock front in a material with a linear viscous rate sensitivity scales as $\eta/(\rho_s c_{\text{pl}})$ where ρ_s is the density of the material and η the viscosity; see Kaliski and Wlodarczyk [14].) In contrast, the front and back face stresses in the $H=6$ mm specimen are approximately equal over the entire deformation history. This is partly due to the smearing of the plastic shock wave and partly a result of the10 μs response time of the measurement system.

The measured peak front and back face stresses (normalized by the corresponding quasi-static peak strength) for the $H=6$ mm

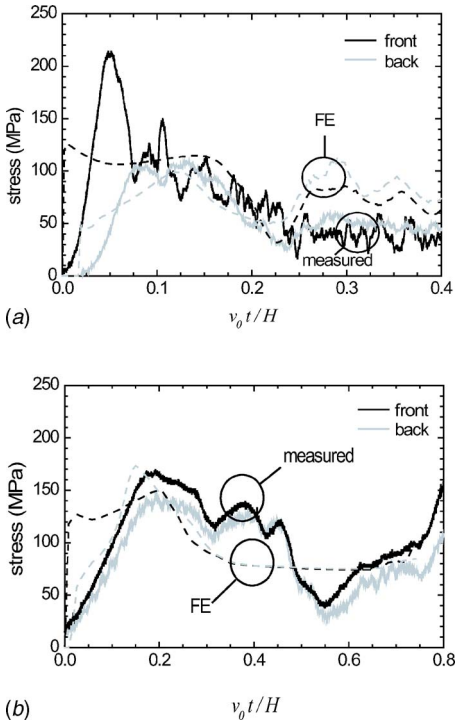

Fig. 10 The measured front and back face stress versus normalised time histories of the (*a*) $H=30$ mm; and (*b*) $H=6$ mm square-honeycomb specimens for an impact velocity $v_o=100$ ms^{-1}. The finite element predictions (constant velocity boundary condition) are included in the figures.

square honeycomb are plotted in Fig. 11 as a function of the impact velocity v_o. Included in Fig. 11 are estimates of the dynamic front and back face stresses based on the material strain-rate sensitivity and the front face stresses due to plastic wave propagation effects, as discussed in Sec. 3.1. (Again, σ_Y in Eq. (5) is interpreted as the yield strength of the solid material at a strain rate $\dot{\varepsilon}^p=10^4$ s^{-1}.) The basic mechanisms of dynamic strength enhancements in these specimens are similar to those in the $H=30$ mm specimens. However, in these shorter specimens, material rate sensitivity smears the plastic shock over the entire height ($H=6$ mm) of the specimen and thus the front and back face

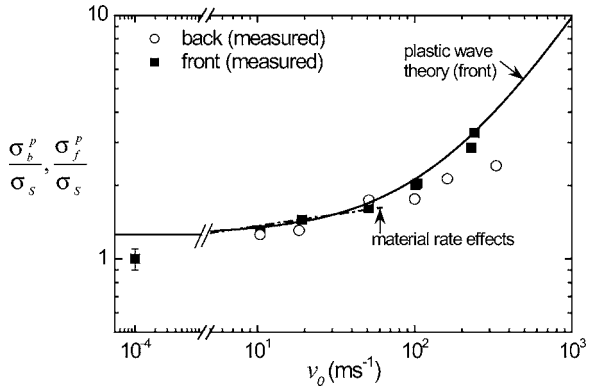

Fig. 11 Measured dynamic peak front (σ_f^p) and back (σ_b^p) face stresses in the $H=6$ mm honeycomb specimens as a function of the impact velocity v_o. The measured dynamic stresses are normalized by peak quasi-static stress σ_s from Fig. 3. The predictions of the dynamic stresses based on material strain-rate sensitivity and one-dimensional plastic wave propagation are included.

stresses are approximately equal over the range of velocities investigated here. Note that the front face stresses for the $H=6$ mm and $H=30$ mm specimens are approximately equal for velocities $v_o>50$ ms^{-1} (Figs. 9 and 11). This confirms that velocity rather than applied nominal strain rate is the governing parameter at these higher rates of compression.

4 Finite Element Investigation

A limited finite element (FE) investigation of the dynamic compression of the square-honeycomb specimens has been performed. The aims of this investigation are:

1. To determine the accuracy of three-dimensional finite element calculations in predicting the dynamic compressive response of the square honeycombs;
2. To use the finite element calculations to investigate the effect of striker deceleration on the measured dynamic response; and
3. To demonstrate the effect of the response time of the measurement system on the measured early time dynamic response of the square honeycombs.

4.1 Three-Dimensional FE Simulations of the Dynamic Compression of the Square Honeycombs. All the FE simulations were conducted using the explicit version of the commercial finite element package ABAQUS. The geometry of the honeycomb specimens was identical to that employed in the experimental investigation and the honeycombs were modeled using linear shell elements (S4R in the ABAQUS notation) with b as the thickness of the honeycomb walls. A mesh sensitivity study showed that an element size of $b/2$ sufficed to give a converged solution. All computations reported here employed such a mesh. Rigid, massless plates (discretized using four-noded rigid elements, R3D4 in the ABAQUS notation) were tied to both the front and back faces of the specimens and the general contact option in ABAQUS was employed to provide hard, frictionless contact between all surfaces in the model. The tie constraint is appropriate if negligible sliding occurs at the interface between the honeycomb and striker mass and Kolsky bar. High-speed photographs of the experiments suggest that this is an appropriate assumption for modeling purposes.

Most of the computations were conducted by compressing the specimen at a constant applied velocity as follows. The front rigid plate was constrained to move only in the axial direction (i.e., in the direction of the height H) of the specimen while the back face was fully clamped. A constant velocity v_o in the axial direction was imposed on the front rigid plate and the axial forces on the front and back faces were monitored as a function of time to determine the front and back face stress versus time history.

In a few simulations, the experimentally applied loadings in the front and back face configurations were also mimicked. In the front face configuration, a point mass M was attached to the back face. The specimen, back face and mass M were then given an initial velocity v_o in the axial direction with the front rigid plate fully clamped and the back face and point mass restricted to move only in the axial direction. Similarly, in the back face configuration, the back face was fully clamped and the point mass (now attached to the front face) was given an initial velocity v_o along with the rigid front plate. The point mass and front plate were constrained to move only in the axial direction.

4.2 Material Properties. It was assumed that the square-honeycomb specimens comprised AISI 304 stainless-steel sheets. Unless otherwise specified, the stainless steel was modeled as J2-flow theory rate dependent solid of density $\rho_f=8060$ kg m^{-3}, Young's modulus $E=210$ GPa and Poisson ratio $\nu=0.3$. The uniaxial tensile true stress versus equivalent plastic strain curves at plastic strain rates 10^{-3} s$^{-1}\leq\dot{\varepsilon}^p\leq10^4$ s^{-1} were tabulated in ABAQUS using the prescription described in Sec. 2.2 and em-

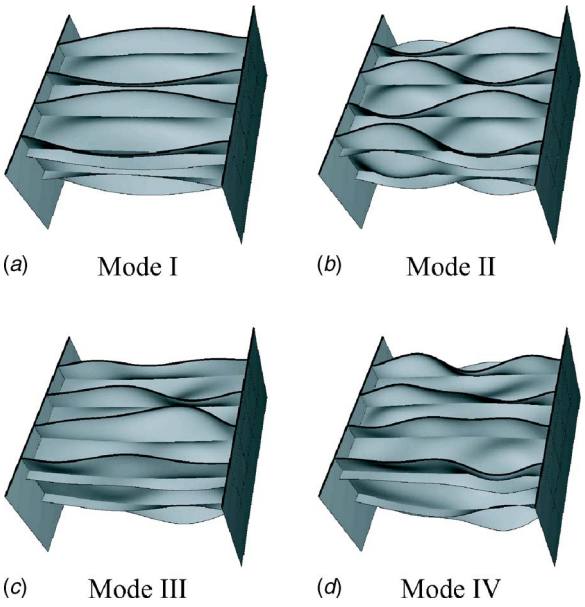

Fig. 12 The four modes of initial imperfections introduced into the FE model of the $H=30$ mm square honeycomb: (*a*) Mode I; (*b*) Mode II; (*c*) Mode III; and (*d*) Mode IV. A section through the midplane of the honeycomb is shown in each case.

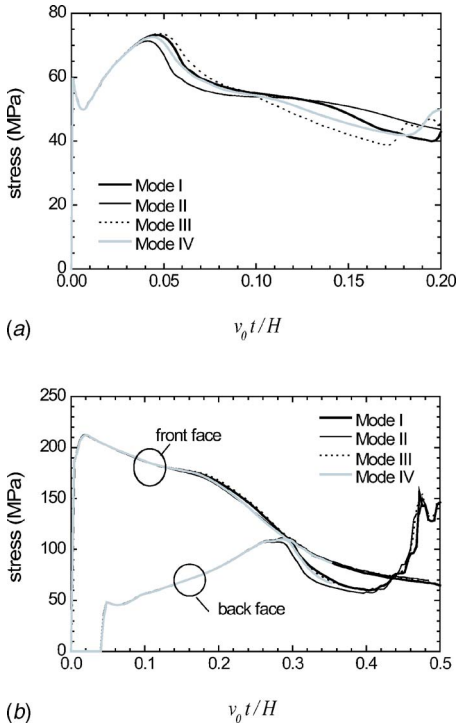

Fig. 13 FE predictions of the front and back face stress versus time histories for the $H=30$ mm compressed at a velocity (*a*) $v_o=20$ ms^{-1} (front face); and (*b*) $v_o=240$ ms^{-1} (front and back face). In both cases, results are shown for the four modes of initial imperfections with an imperfection amplitude $0.05b$.

ploying the data of Fig. 2.

A comparison between the quasi-static FE predictions and measurements is included in Fig. 3; see Zok et al. [15] for details of such calculations and reasons for the discrepancies between the measurements and the FE predictions.

4.3 Effect of Initial Imperfections. The effect of initial imperfections on the finite element predictions of the dynamic compressive response was first investigated. Dynamic compression typically results in the activation of higher order buckling modes as seen in the high-speed photographs presented above. The buckling wavelengths are a strong function of the material properties and compression velocity as discussed by Abrahamson and Goodier [12] for the dynamic buckling of rods. Consequently, we investigated the effect of the magnitude and mode of imperfection on the dynamic compressive response of the square honeycombs.

Four modes of initial imperfections were considered. Modes I and II are the two lowest static eigenmodes with the Mode II wavelength half that of Mode I. In order to investigate the effect of a distribution of imperfection wavelengths we also considered modes which are the sum of the first 20 and 40 static eigenmodes (equal maximum amplitude for each mode). These will be subsequently referred to as Modes III and IV, respectively. All four modes are shown in Fig. 12 for the $H=30$ mm honeycomb.

The FE predictions of the stress versus time histories of the $H=30$ mm honeycomb for applied velocities $v_o=20$ ms^{-1} and 240 ms^{-1} are plotted in Figs. 13(*a*) and 13(*b*), respectively. The front and back face stresses are almost equal for $v_o=20$ ms^{-1} and thus for the sake of clarity only the front face stresses are shown in Fig. 13(*a*). In each case, results are plotted for the four initial imperfection modes with a maximum imperfection amplitude of $0.05b$. We observe that the choice of the initial imperfection mode has a negligible effect on the predicted stress versus time histories. In fact, for the range of compressive velocities considered here, the FE calculations predict a response that is insensitive to the mode of the imperfections for imperfection amplitudes in the range $0.02b-0.1b$. This holds for both the $H=30$ mm and $H=6$ mm honeycombs. All the calculations reported subsequently employ the Mode I imperfection with a maximum imperfection amplitude of $0.05b$.

4.4 Sensitivity of Response to Choice of Loading Condition. The striker mass M in the experiments was chosen to give an approximately uniform compression velocity over a nominal compressive strain of about 40%. Here we employ FE calculations to verify this and also to compare the FE predictions of the striker velocity over the deformation history of the specimens with those inferred from measurements.

FE predictions of the front and back face stresses of the $H=30$ mm square honeycomb with $v_o=20$ ms^{-1} are shown in Fig. 14 for constant velocity compression and for projectile impact with a given initial velocity. In the impact simulations, a point mass $M=2.4$ kg was attached to the square honeycomb to represent the striker employed in the experiments. Both sets of FE predictions are nearly identical for $v_o t/H<0.2$ with small discrepancies between the two sets of simulations for $v_o t/H>0.2$.

We proceed to estimate the velocity reduction of the striker in the experiments and to compare these estimates with the FE pre-

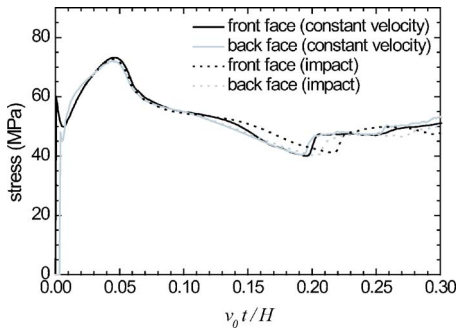

Fig. 14 A comparison between the FE predictions for a constant applied velocity and for impact boundary conditions ($H=30$ mm honeycomb specimen with $v_o=20$ ms^{-1})

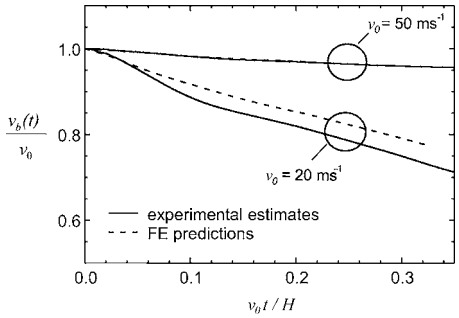

Fig. 15 Experimental estimates and FE predictions of the normalized striker velocity $v_b(t)/v_o$ as a function of the normalized time $v_o t/H$ for the back face configuration with initial striker velocities of v_o=20 ms^{-1} and 50 ms^{-1}

dictions. This reduction is most severe in the back face configuration since the striker is decelerated by a force associated with driving along the plastic shock wave. The striker velocity versus time relation in the back face configuration is given by

$$v_b(t) = v_o - \frac{1}{M}\int_0^t F_f\, dt \tag{6}$$

where F_f is the measured force exerted by the square-honeycomb specimens in the corresponding front face configuration. The normalized striker velocity $v_b(t)/v_o$ (inferred from measurements) in the back face configuration of the H=30 mm specimens are plotted in Fig. 15 as a function of the normalized time $v_o t/H$ for the v_o=20 ms^{-1} and 50 ms^{-1} cases. These calculations were performed with M=2.4 kg to match the striker mass employed in the experiments. It is clear from Fig. 15 that, while there is a negligible reduction in velocity for the v_o=50 ms^{-1} case, the velocity of the striker reduces by about 20% for the v_o=20 ms^{-1} case at $v_o t/H \approx 0.35$. The corresponding FE predictions of the striker velocity in the back face configuration are included in Fig. 15 (measured directly from the velocity of the point mass in the FE calculations). The FE calculations predict slightly less velocity reductions than those estimated from the experimental measurements. This is likely to be related to the "ringing" in the experimental measurements which results in an overestimation of the front face force. Similar estimates for the other impact velocities confirmed that negligible striker velocity reductions occurred in all experiments with $v_o > 50$ ms^{-1}. These experimental estimates and FE predictions confirm that the impact experiments can be regarded as constant velocity experiments over the practical deformation regime $0 < v_o t/H < 0.4$.

4.5 Accuracy of Predictions for the H=30 mm Square Honeycombs. FE predictions of the front and back face stresses on the H=30 mm specimens are included in Figs. 6(*a*), 7(*a*), and 8(*a*) for a constant velocity of v_o=20 ms^{-1}, 50 ms^{-1}, and 240 ms^{-1}, respectively. The simulations were terminated within the FE code when large rotations of the shell elements resulted in a loss of accuracy of the simulations. The FE simulations capture the measured stresses in the v_o=20 ms^{-1} and 50 ms^{-1} experiments to reasonable accuracy. The FE predictions of the deformation mode for the v_o=50 ms^{-1} case are plotted in Fig. 16 at t=55 μs and 155 μs. It is noted that the observed deformation (Fig. 7(*b*)) and predicted deformation modes (Fig. 16) are quite different; a similar discrepancy in deformation mode was observed for v_o =20 ms^{-1} although the comparison is not shown explicitly. This discrepancy is likely to be associated with the tearing of the brazed joints in the experiments (and not accounted for in the FE calculations). Important differences between the measured and FE predictions of the compressive response at v_o=20 ms^{-1} and

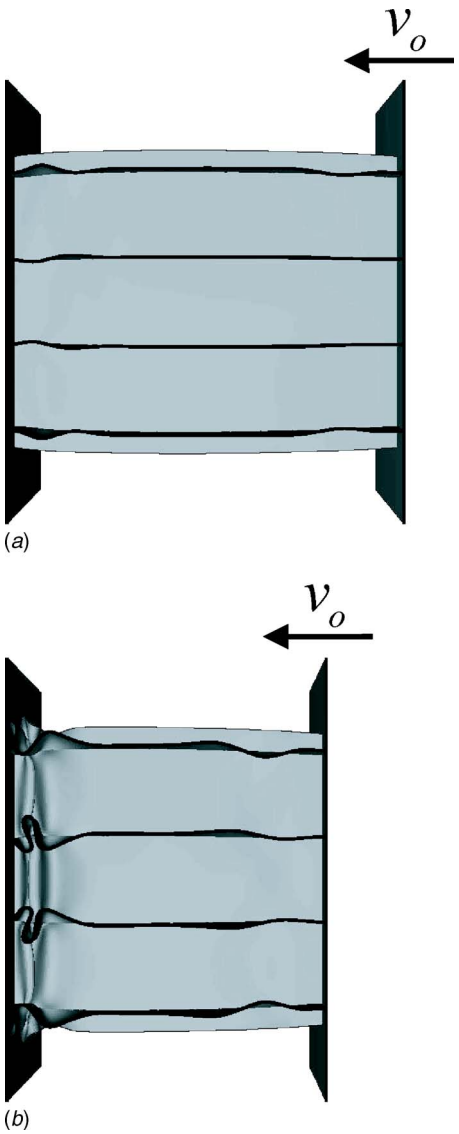

Fig. 16 The FE predictions of the deformation mode of the H =30 mm honeycomb specimen, subjected to a constant applied velocity v_o=50 ms^{-1} at: (*a*) t=55 μs; and (*b*) t=155 μs. These times correspond to the times of the high speed photographs in Fig. 7(*b*). A section through the midplane of the honeycomb is shown.

50 ms^{-1} are as follows.

1. The FE simulations predict a sharp rise of the stresses on the front and back faces due to the presence of the elastic stress wave. Such a sharp rise is not observed in the experiments. This is likely to be related to the fact that the response time of the measurement apparatus is about 10 μs and thus the experimental measurements are unable to capture the instantaneous rise in stress due to the arrival of the elastic wave.

2. At $v_o t/H \approx 0.20$, the FE simulations predict a sudden increase in the stresses on the back face due to contact between the cell walls as seen in Fig. 16 for the v_o=50 ms^{-1} simulation. In reality, a much gentler increase in the measured stresses occurs. We attribute this discrepancy to tearing of the brazed joints of the square honeycombs as evidenced from the dust clouds in the photograph at t=255 μs in Fig. 8(*b*). This effect is not included in the FE simulations and is likely to result in an overprediction of the measured stress.

The comparisons between the FE simulations and measurements for the v_o=240 ms^{-1} case (Fig. 8(*b*)) show larger discrep-

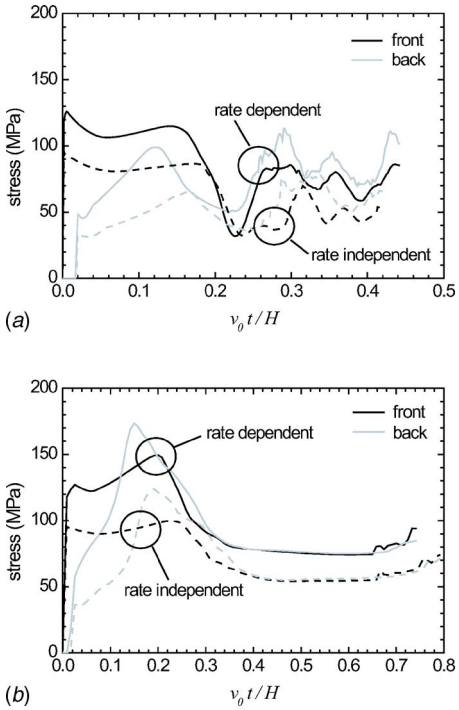

Fig. 17 Comparisons between the rate independent and rate dependent FE predictions (constant applied velocity) of the front and back face stresses: (*a*) $H=30$ mm; and (*b*) $H=6$ mm square-honeycombs, for $v_o=100$ ms^{-1}

ancies. The differences between the measurements and predictions of the stresses are mainly due to the slow response time of the measurement apparatus, with the predictions and measurements in reasonable agreement for $v_o t/H > 0.2$. The oscillations in the measured stress history are due to flexural waves induced in the Kolsky bar by slight misalignment of the impact and are neglected in the FE simulations. Again, the FE calculations predict a rise in the back face stress at $v_o t/H \approx 0.4$. This rise is not observed in the experiments due to tearing of the brazed joints of the specimens.

4.6 FE Simulations to Elucidate the Role of Material Rate Sensitivity. The measurements indicate that the plastic wave reaches the distal end of the specimen earlier than predicted by rate independent, small strain plasticity theory. For example, with a plastic wave speed of $c_{pl} \approx 410$ ms^{-1} and an input speed of $v_o = 100$ ms^{-1}, it is predicted that the plastic wave will increase the stress on the back face to 100 MPa at $v_o t/H \approx 0.25$. However, the measurements in Fig. 10 suggest that the plastic wave arrives much earlier, at $v_o t/H \approx 0.1$. The FE predictions are in reasonable agreement with the experimental measurements for $t > 10$ μs, that is for $v_o t/H > 0.01$ and 0.03 for the $H=30$ mm and 6 mm specimens, respectively. This confirms that the high stress measurements over $0.1 < v_o t/H < 0.25$ are not an artefact of the measurement system but are probably related to an increased plastic wave speed associated with the rate sensitivity of the 304 stainless steel.

We proceed to check the effect of material rate sensitivity by performing FE simulations with the 304 stainless steel modeled as a rate independent J2 flow theory solid with a uniaxial tensile stress versus plastic strain response given by the $\dot{\varepsilon}^p = 10^{-3}$ s^{-1} data in Fig. 2(*a*). A comparison between the rate independent and rate dependent FE predictions (constant applied velocity) of the front and back face stresses on $H=30$ mm and 6 mm square honeycombs is shown in Figs. 17(*a*) and 17(*b*), respectively, for $v_o = 100$ ms^{-1}. The rate dependent and rate independent FE calculations predict that the plastic wave arrives at the back face at $v_o t/H \approx 0.15$ and $v_o t/H \approx 0.2$, respectively. Thus, the FE calculations demonstrate that material strain rate sensitivity can account for the increased plastic wave speed. The dynamic strength enhancement due to material rate effects are also clearly seen in Fig. 17: the rate dependent FE calculations predict that both the front and back face stresses are about 25% higher than those in the rate independent case.

5 Concluding Remarks

Square-honeycomb specimens of relative density $\bar{\rho}=0.10$ and heights $H=30$ mm and 6 mm were manufactured by slotting together 304 stainless-steel sheets and then brazing together the assembly. The out-of-plane compressive response of these specimens was measured for velocities ranging from quasi-static values to $v_o = 300$ ms^{-1}. The stresses on both the front and back faces of the square honeycombs were measured in the dynamic tests using a direct impact Kolsky bar.

Torsional plastic buckling of the webs is the collapse mode under quasi-static loading. Three distinct mechanisms govern the dynamic response of the square honeycombs: (i) material rate sensitivity; (ii) inertial stabilization of the webs against buckling; and (iii) plastic wave propagation. In the $H=30$ mm specimens, effects (i) and (ii) are dominant for $v_o < 50$ ms^{-1} with the front and back face stresses increasing by about a factor of two over their quasi-static values. At higher velocities, plastic wave effects become increasingly important with the back face stress remaining approximately constant at its value for $v_o = 50$ ms^{-1} and the front face stress increasing approximately linearly with velocity. The peak front face stresses in the $H=6$ mm and $H=30$ mm cases are approximately equal at the higher velocities indicating that velocity rather than strain rate governs the response of these specimens under high rates of compression.

Three-dimensional finite element simulations capture the experimental measurements to reasonable accuracy. Discrepancies between the measurements and predictions are attributed to: (i) a response time of 10 μs by the measurement apparatus; and (ii) tearing of the square honeycombs along the brazed joints. This tearing leads to a significant drop in the transmitted load and in the energy absorbed by the square honeycomb.

Acknowledgment

The authors are grateful to ONR for their financial support through US-ONR IFO Grant No. N00014-03-1-0283 on The Science and Design of Blast Resistant Sandwich Structures and to the Isaac Newton Trust, Trinity College Cambridge.

References

[1] Fleck, N. A., and Deshpande, V. S., 2004, "The Resistance of Clamped Sandwich Beams to Shock Loading," J. Appl. Mech., **71**, pp. 386–401.
[2] Xue, Z., and Hutchinson, J. W., 2004, "A Comparative Study of Blast-Resistant Metal Sandwich Plates," Int. J. Impact Eng., **30**, pp. 1283–1305.
[3] Radford, D. D., Fleck, N. A., and Deshpande, V. S., 2005, "The Response of Clamped Sandwich Beams Subjected to Shock Loading," Int. J. Impact Eng., **32**, pp. 968–987.
[4] McShane, G. J., Radford, D. D., Deshpande, V. S., and Fleck, N. A., 2006, "The Response of Clamped Sandwich Plates With Lattice Cores Subjected to Shock Loading," Eur. J. Mech. A/Solids, **25**, pp. 215–229.
[5] Zhao, H., and Gary, G., 1998, "Crushing Behaviour of Aluminium Honeycombs Under Impact Loading," Int. J. Impact Eng., **21**, pp. 827–836.
[6] Wu, E., and Jiang, W-S., 1997, "Axial Crush of Metallic Honeycombs," Int. J. Impact Eng., **12**, pp. 439–456.
[7] Harrigan, J. J., Reid, S. R., and Peng, C., 1999, "Inertia Effects in Impact Energy Absorbing Materials and Structures," Int. J. Impact Eng., **22**, pp. 955–979.
[8] Xue, Z., and Hutchinson, J. W., 2005, "Crush Dynamics of Square-Honeycomb Sandwich Cores," submitted.

[9] Côté, F., Deshpande, V. S., Fleck, N. A., and Evans, A. G., 2004, "The Out-of-Plane Compressive Behaviour of Metallic Honeycombs," Mater. Sci. Eng., A, **380**, pp. 272–280.
[10] Stout, M. G., and Follansbee, P. S., 1986, "Strain-Rate Sensitivity, Strain Hardening, and Yield Behaviour of 304L Stainless Steel," J. Eng. Mater. Technol., **108**, pp. 344–353.
[11] Dharan, C. K. H., and Hauser, F. E., 1970, "Testing Techniques Based on the Split Hopkinson Bar," Exp. Mech., **10**, pp. 370–376.
[12] Abrahamson, G. R., and Goodier, J. N., 1966, "Dynamic Flexural Buckling of Rods Within an Axial Plastic Compression Wave," J. Appl. Mech., **33**, pp. 241–247.
[13] Calladine, C. R., and English, R. W., 1984, "Strain-Rate and Inertia Effects in the Collapse of Two Types of Energy-Absorbing Structure," Int. J. Mech. Sci., **26**, pp. 689–701.
[14] Kaliski, S., and Wlodarczyk, E., 1967, "On Certain Closed-Form Solutions of the Propagation and Reflection Problem of an Elastic-Visco-Plastic Wave in a Bar," Arch. Mech. Stosow., **19**, pp. 433–452.
[15] Zok, F. W., Rathbun, H., He, M., Ferri, E., Mercer, C., McMeeking, R. M., and Evans, A. G., 2005, "Structural Performance of Metallic Sandwich Panels With Square-Honeycomb Cores," Philos. Mag., **85**, pp. 3207–3234.